minerals

MDPI

Article

Three-Dimensional Regularized Focusing Migration: A Case Study from the Yucheng Mining Area, Shandong, China

Yidan Ding [1,*], Guoqing Ma [1,*], Shengqing Xiong [2] and Haoran Wang [1]

[1] College of Geo-Exploration Sciences and Technology, Jilin University, Changchun, 130000, China
[2] China Aero-Geophysical Survey and Remote Sensing center for Land and Resources, Beijing, 100083, China
* Correspondence: dingyd@jlu.edu.cn; maguoqing@jlu.edu.cn

Received: date; Accepted: date; Published: date

Abstract: Gravity migration is a fast imaging technique based on the migration concept to obtain subsurface density distribution. For higher resolution of migration imaging results, we propose a 3D regularized focusing migration method that implements migration imaging of entire gravity surveys with focusing stabilizer based on regularization theory. When solving the model parameters, the iterative direction is chosen as the conjugate migration direction, and the iterative step size is selected on the basis of Wolfe-Powell conditions. The model tests demonstrate the proposed method can improve the resolution and precision of imaging results, especially for block structures. At the same time, the method has high computational efficiency, which allows a rapid imaging for large scale gravity data. It also has high stability in noise conditions. The developed novel method is applied to interpret the gravity survey data collected in a skarn-type iron deposit in Yucheng, Shandong province. Migration results show that the buried depth of iron ore in this area is 750-1500 m, which is consistent with the actual drilling data. We also put forward suggestions for further mineral exploration in the survey area. This method can be used to complete rapid global imaging of large mining areas and provide important technical support for exploration of deep concealed deposits.

Keywords: 3D focusing migration; regularization; conjugate migration direction; fast imaging; skarn-type iron deposits

1. Introduction

Gravity exploration that can effectively obtain the comprehensive response of subsurface density distribution is an important method in geophysical exploration and is widely used in estimating target mineralized zones. Subsurface density distribution can be obtained by the inversion of gravity data, but from the perspective of classical theory, all geophysical inversions including gravity inversion are ill-posed for their solutions are either non-unique or unstable. Nevertheless, geophysicists can solve this problem to some extent by adopting different types of regularization algorithms. Tikhonov [1] established regularization theory (also see [2,3,4]). The regularized inversion problem can be solved by an optimization problem of finding a solution that minimizes the objective functional which can be expressed as

$$P(\boldsymbol{m}) = P_d(\boldsymbol{m}) + \lambda P_m(\boldsymbol{m}), \quad (1)$$

where $P_d(m)$ is the misfit functional, $P_m(m)$ is the stabilizing functional that can make the inversion inversion result contain a priori information of the model parameters, and λ is the regularization parameter that balances the effects of $P_d(m)$ and $P_m(m)$.

On the basis of this equation, varieties of 3D regularized inversion methods for gravity data were developed with different regularization terms, such as regularized smooth inversion based on the L2 norm (e.g., [5,6]), sparse inversion based on the L1 norm (e.g., [7]), elastic-net inversion (e.g., [8]), total variation inversion (e.g., [9,10]) and focusing inversion (e.g., [11,12]). Several classical techniques were also developed to automatically estimate an appropriate regularization parameter [13-15]. They have different effects and scopes of application [16,17].

Considering the calculation ~~amount and time~~, inversion methods may ~~face the inability of efficiency~~ in actual data processing, and cannot complete the overall 3D density imaging of large regions. Such inefficiency of inversion has become a bottleneck in the study of regional structure and deep geological problems. Therefore, it is an urgent problem to improve computing efficiency. Zhdanov introduced the concept of potential field migration and demonstrated its application for rapid 2D and 3D imaging ~~of entire~~ gravity ~~or~~ gradiometry surveys [18-21]. For gravity and its gradient field, migration imaging is based on the direct integral transformation of gravity and its gradient data (that can also be mathematically described as the action of the adjoint operator on the observed data). The potential field migration method is fast and stable, and can be used for real-time imaging. However, ~~its~~ imaging results ~~are~~ divergent. Later, this method was extended to iterative migration [22], in which case adjoint operators were iteratively used. ~~That is to say, the~~ forward model is introduced to estimate the accuracy of the migration results by computing the residual of observed data and ~~prospected~~ data during each iteration. When the residual is less than a given value, this migration imaging model is adopted as the final result. In this way, imaging accuracy is improved. Multi-component joint iterative migration, which was subsequently developed, further improved vertical resolution [23].

The potential field migration method instantaneously provides an estimation ~~to~~ density distribution in a single step, while iterative migration improves spatial resolution. However, the introduction of an iterative process reduces ~~its~~ efficiency. In order to maintain the high efficiency of migration and improve the resolution and stability, we propose ~~a~~ method called 3D regularized focusing migration. We introduce an objective functional similar to that of regularized inversion. We select the focusing stabilizer based on the form adopted by Portniaguine and Zhdanov [24], which helps to generate a sharp and focused image of the model. We follow the regularization parameter selection criterion on the basis of Portniaguine et al. [25], that is, the regularization parameter is given an initial value, and then successively decreases in iterative calculation, thus accelerating convergence and robustness. When solving the optimization problem of minimizing the objective functional, the search direction of our algorithm is the conjugate migration direction instead of the conjugate gradient direction for conventional regularized inversion. Good results can be obtained at the first migration, that is, the predicted anomaly of model parameters obtained in the first migration has a relatively consistent shape with the observed anomaly. Using the conjugate migration direction results in faster convergence than ~~using~~ the conjugate gradient direction ~~in inversion~~. ~~So we~~ can obtain relatively convergent results with fewer iterations. Unfortunately, line searches are still performed multiple times ~~in~~ minimizing the objective functional. In order to improve line search efficiency under the premise of ensuring algorithm convergence, the iterative step size is selected based on the inexact line search step size criterion proposed by Wolfe and Powell [26,27]. When the model scale is relatively large, adopting the Wolfe-Powell conditions allows a misfit to consume less time to reach ~~the~~ given ~~value~~.

The proposed method is efficient and stable, and can provide ~~real-time~~ high-resolution subsurface density distribution ~~imaging~~. It is well suited for evaluating mining targets, because our efficient algorithm allows fast imaging without being constrained by millions of data~~sets~~ over large mining areas. Our regularization parameter selection criterion is applicable for the ~~very~~ case when the observed data are contaminated with Gaussian noise of uniform but unknown standard deviation just as the real data collected. The focusing stabilizer can distinguish the boundary of each geological body as ore bodies ~~are mostly concentrated in relatively high density~~.

In the following sections, we briefly introduce the principle of regularized focusing migration method, and ~~use~~ synthetic models to verify the rationality and performance of our method. Then it

is applied to the interpretation of gravity data collected ~~from~~ Yucheng, Shandong province ~~which~~ has been proved to have ~~great~~ potential mining targets for skarn-type iron ore deposits ~~but~~ with no surface expressions. We discuss the geological background of this area, interpret ~~the~~ ~~geophysical~~ data, and provide a road map for further mineral exploration.

2. Methodology

2.1. Forward Modeling of Gravity Anomalies

The purpose of gravity forward modeling is to calculate the effect of subsurface density distribution on the observation surface. The modelling domain is discretized into rectilinear cuboids of constant density (Figure 1). Discrete forward modelling for gravity anomalies produced by arbitrary density distribution can be expressed in general matrix notation as:

$$\boldsymbol{d} = \boldsymbol{A}\boldsymbol{m}, \tag{2}$$

where $\boldsymbol{d}$ is a vector of the observed data of order n; $\boldsymbol{m}$ is a vector of the model parameters of order m; $\boldsymbol{A}$, called the sensitivity matrix, is a matrix of size n by m formed by the corresponding gravity field kernels. If the subsurface modelling region is divided into $n_x \times n_y \times n_z$ geometric cuboids, then $n = n_x \times n_y, m = n_x \times n_y \times n_z$.

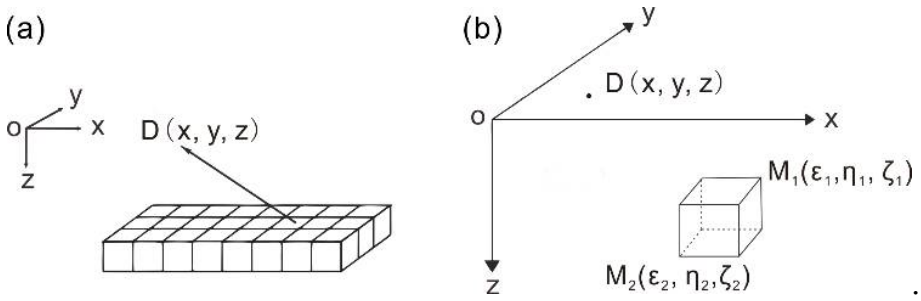


Figure 1. ~~Interpretation models~~ (a) A layer of rectilinear cuboids; (b) a single cuboid. Observation position is described by coordinate ~~triple~~ (x, y, z). Coordinates of cuboid corners can be completely described by two ~~triples~~ $(\varepsilon_1, \eta_1, \zeta_1)$ and $(\varepsilon_2, \eta_2, \zeta_2)$.

The gravity anomalies generated by any geometric cuboid M at observation point D can be expressed as [28].

$$\boldsymbol{d} = \gamma\rho_M \left\{(\varepsilon - x)In[R - (\eta - y)] + (\eta - y)In[R - (\varepsilon - x)] - (\zeta - z)\tan^{-1}\frac{(\varepsilon - x)(\eta - y)}{(\zeta - z)R}\right\}\Bigg|_{\varepsilon_1}^{\varepsilon_2}\Bigg|_{\eta_1}^{\eta_2}\Bigg|_{\zeta_1}^{\zeta_2}, \tag{3}$$

where γ is the gravitational constant; ρ_M is the density of the geometric cuboid; (x, y, z) are the coordinates of surface observation point and ε_1, ε_2, η_1, η_2, ζ_1, ζ_2 are coordinates to determine the the subdivision cuboid space. $R = \sqrt{(\varepsilon - x)^2 + (\eta - y)^2 + (\zeta - z)^2}$.

2.2. Principles of of Gravity Field Migration

Given that gravity field dataset $\boldsymbol{d}^{obs}$ is observed on the observation surface S, the ~~question~~ is ~~how~~ to determine the subsurface density distribution $\boldsymbol{m}$. Zhdanov proposed a migration imaging method ~~that can perform fast imaging~~ on the basis of Newton method. Its imaging principle is described briefly below [29].

In the framework of Newton method, a solution to the problem of parameter functional minimization can be found in one step siz When both the initial model and the prior model of ~~abnormal~~ density distribution are equal to zero, the solution can be expressed as:

$$\boldsymbol{m} = -\frac{1}{\lambda}(\boldsymbol{W}_{\boldsymbol{m}}^{*}\boldsymbol{W}_{\boldsymbol{m}})^{-1}\boldsymbol{l}_{\boldsymbol{0}}, \tag{4}$$

where λ is the regularization parameter; $\boldsymbol{W}_{\boldsymbol{m}}$ is a model weighting matrix; $\boldsymbol{l}_{\boldsymbol{0}}$ is the direction of steepest descent that is introduced as a result of applying adjoint gravity operator, $\boldsymbol{A}^{*}$, to the observed observed gravity data, $\boldsymbol{d}^{\boldsymbol{obs}}$:

$$\boldsymbol{l}_{\boldsymbol{0}} = -\boldsymbol{A}^{*}\boldsymbol{d}^{\boldsymbol{obs}}, \tag{5}$$

where adjoint gravity operator, $\boldsymbol{A}^{*}$, is specified as

$$\boldsymbol{A}^{*} = \gamma \iint \frac{\boldsymbol{d}}{|\boldsymbol{r}'-\boldsymbol{r}|^{3}}(\boldsymbol{z}'-\boldsymbol{z})ds. \tag{6}$$

Let $\frac{1}{\lambda} = k_{\alpha}$, and substitute Equation (5) into Equation (4), migration density can be rewritten as

$$\boldsymbol{m} = k_{\alpha}(\boldsymbol{W}_{\boldsymbol{m}}^{*}\boldsymbol{W}_{\boldsymbol{m}})^{-1}\boldsymbol{A}^{*}\boldsymbol{d}^{\boldsymbol{obs}} = k_{\alpha}\boldsymbol{\omega}_{\boldsymbol{\alpha}}^{\boldsymbol{2}}\boldsymbol{A}^{*}\boldsymbol{d}^{\boldsymbol{obs}}. \tag{7}$$

Weighting operator, $\boldsymbol{\omega}_{\boldsymbol{\alpha}}$, is constructed based on the square root of the integrated sensitivity of the data to the density, $\boldsymbol{S}_{\boldsymbol{\alpha}}$:

$$\boldsymbol{\omega}_{\boldsymbol{\alpha}} = \sqrt{\boldsymbol{S}_{\boldsymbol{\alpha}}}. \tag{8}$$

Unknown coefficient, k_{α}, can be determined by linear line search:

$$k_{\alpha} = \frac{\|\boldsymbol{A}^{\boldsymbol{\omega}}\boldsymbol{A}^{\boldsymbol{\omega}*}\boldsymbol{d}^{\boldsymbol{obs}}_{\boldsymbol{\alpha}}\|^{2}}{\|\boldsymbol{A}^{\boldsymbol{\omega}}_{\boldsymbol{\alpha}}\boldsymbol{A}^{\boldsymbol{\omega}*}_{\boldsymbol{\alpha}}\boldsymbol{d}^{\boldsymbol{obs}}_{\boldsymbol{\alpha}}\|^{2}}. \tag{9}$$

Migration gives us a method to analytically solve for model parameters, so rather than ~~needing to run~~ an iterative algorithm, we ~~can instead just~~ solve for the optimal value for $\boldsymbol{m}$ ~~all at one go~~. It is obvious that migration cannot obtain relatively accurate imaging results, although it has great advantages in terms of efficiency. ~~To this end~~, the regularized focusing migration method is introduced in this paper. ~~The specific principle is as follows.~~

2.3. Regularized Focusing Migration

We can consider k_{α} in ~~Formula~~ (7) as ~~the~~ step size and $\boldsymbol{\omega}_{\boldsymbol{\alpha}}^{\boldsymbol{2}}\boldsymbol{A}_{\boldsymbol{\alpha}}^{*}$ as the migration direction, ~~in which case~~ migration is similar to the first iteration of a general inversion problem.

In regularization theory, the solution of linear inverse problem (2) is substituted by minimization of Tikhonov objective functional:

$$P(m) = \|\boldsymbol{W}_{\boldsymbol{d}}(\boldsymbol{A}\boldsymbol{m}-\boldsymbol{d})\|^{2} + \lambda\left\|\boldsymbol{W}_{\boldsymbol{m}}\left(\boldsymbol{m}-\boldsymbol{m}_{\boldsymbol{apr}}\right)\right\|^{2} \rightarrow min, \tag{10}$$

where $\boldsymbol{m}_{\boldsymbol{apr}}$ is a prior model; and $\boldsymbol{W}_{\boldsymbol{d}}$, $\boldsymbol{W}_{\boldsymbol{m}}$, are weighting matrices of the data and model parameters, respectively.

We introduce a focusing weighting matrix $\boldsymbol{W}_{\boldsymbol{e}}$, and the reweighted objective functional can be rewritten as:

$$P_{\alpha}(\boldsymbol{m}^{\boldsymbol{\omega}},\ \boldsymbol{d}^{\boldsymbol{\omega}}) = \|\ \boldsymbol{A}^{\boldsymbol{\omega}}\boldsymbol{m}^{\boldsymbol{\omega}} - \boldsymbol{d}^{\boldsymbol{\omega}}\ \|^{2} + \lambda\ \|\ \boldsymbol{m}^{\boldsymbol{\omega}}\ \|^{2}, \tag{11}$$

where

$$\boldsymbol{A}^{\boldsymbol{\omega}} = \boldsymbol{W}_{\boldsymbol{d}}\boldsymbol{A}\boldsymbol{W}_{\boldsymbol{m}}{}^{-\boldsymbol{1}}\boldsymbol{W}_{\boldsymbol{e}}{}^{-\boldsymbol{1}}, \tag{12}$$

$$\boldsymbol{d}^{\boldsymbol{\omega}} = \boldsymbol{W}_{\boldsymbol{d}}\boldsymbol{d}, \tag{13}$$

$$\boldsymbol{m}^{\boldsymbol{\omega}} = \boldsymbol{W}_{\boldsymbol{e}}\boldsymbol{W}_{\boldsymbol{m}}\boldsymbol{m}. \tag{14}$$

There are different choices of weighting matrices $\boldsymbol{W}_{\boldsymbol{e}}$, $\boldsymbol{W}_{\boldsymbol{d}}$, $\boldsymbol{W}_{\boldsymbol{m}}$. Here we choose the following forms:

$$\boldsymbol{W}_{\boldsymbol{e}} = diag\frac{1}{\sqrt{(\boldsymbol{m})^{2}}}, \tag{15}$$

$$\boldsymbol{W_d} = diag(\boldsymbol{AA^T})^{\frac{1}{2}}, \tag{16}$$

$$\boldsymbol{W_m} = diag(\boldsymbol{A^T A})^{\frac{1}{2}}. \tag{17}$$

For the n th iteration (n=1, 2, 3...), the objective functional can be written as:

$$P_{\alpha_n}(\boldsymbol{m_n^{\omega_n}}, \ \boldsymbol{d^{\omega_n}}) = \| \boldsymbol{A^{\omega_n} m_n^{\omega_n}} - \boldsymbol{d^{\omega_n}} \|^2 + \lambda_n \| \boldsymbol{m_n^{\omega_n}} \|^2. \tag{18}$$

When solving the model parameters, different from the conjugate gradient method ~~used~~ in the general inversion problem, ~~we~~ provide the conjugate migration direction method, that ~~is~~, the search direction of each iteration is along the conjugate migration direction. Then for regularized migration, according to ~~Formula~~ (5) , we define the migration direction as

$$\boldsymbol{l_m} = \boldsymbol{A^{\omega_n *}}\left(\boldsymbol{A^{\omega_n} m_n^{\omega_n}} - \boldsymbol{d^{\omega}}\right) + \lambda_n\left(\boldsymbol{m_n^{\omega_n}}\right), \tag{19}$$

and the conjugate migration direction is defined as the linear combination of the migration direction on this step and the conjugate migration direction ~~on~~ the previous step. Hence the conjugate migration direction for current model parameter $\boldsymbol{m_n^{\omega_n}}$ is:

$$\tilde{\boldsymbol{I}}_{\boldsymbol{n}}^{\boldsymbol{\omega_n}} = \boldsymbol{I_n^{\omega_n}} + \beta_n \tilde{\boldsymbol{I}}_{\boldsymbol{n}}^{\boldsymbol{\omega_{n-1}}}, \tag{20}$$

where

$$\boldsymbol{I_n^{\omega_n}} = \boldsymbol{A^{\omega_n *}}\left(\boldsymbol{A^{\omega_n} m_n^{\omega_n}} - \boldsymbol{d^{\omega}}\right) + \lambda_n\left(\boldsymbol{m_n^{\omega_n}}\right), \tag{21}$$

$$\beta_n = \frac{\| \boldsymbol{I_n^{\omega_n}} \|^2}{\| \boldsymbol{I_{n-1}^{\omega_{n-1}}} \|^2}. \tag{22}$$

Specifically, the conjugate migration direction is defined as the migration direction when n = 0, namely $\tilde{\boldsymbol{I}}_{\boldsymbol{0}}^{\boldsymbol{\omega_0}} = \boldsymbol{I_0^{\omega_0}}$.

The successive line search in the conjugate migration direction can be written as:

$$\boldsymbol{m_{n+1}^{\omega_n}} = \boldsymbol{m_n^{\omega_n}} - k_n \tilde{\boldsymbol{I}}_{\boldsymbol{\alpha_n}}^{\boldsymbol{\omega_n}}. \tag{23}$$

Here, k_n is the iteration step ~~size~~. We take the Wolfe-Powell inexact line search conditions instead of of the exact line search criterion shown in ~~Formula~~ (9) of the conventional iterative migration to obtain the step size [30], that is, for each iteration the method first finds ~~an interval of~~ the step size, and then finds the parameters that satisfy the conditions where the step size brings about a sufficient reduction for the value of the objective functional using a stepwise dichotomy method. One can find the formal proof of convergence of this type of optimization technique in [27].

The actual model parameters can be converted as

$$\boldsymbol{m_{n+1}} = \boldsymbol{W_m}^{-1} \boldsymbol{W_{e_n}}^{-1} \boldsymbol{m_{n+1}^{\omega_n}}, \tag{24}$$

where $\boldsymbol{W_{e_n}}$ is the focusing weighting matrix updated according to the $\boldsymbol{m_n}$ obtained on the $(n-1)$st iteration.

Reweight $\boldsymbol{m_{n+1}}$ to get $\boldsymbol{m_{n+1}^{\omega_{n+1}}}$:

$$\boldsymbol{m_{n+1}^{\omega_{n+1}}} = \boldsymbol{W_m W_{e_{n+1}} m_{n+1}}. \tag{25}$$

To ensure that the misfit functional converges to the global minimum, the following procedures are adopted to reduce the regularization factor. First, let

$$p_n = \frac{\| \boldsymbol{m_{n+1}^{\omega_{n+1}}} \|^2}{\| \boldsymbol{m_n^{\omega_n}} \|^2}, \tag{26}$$

and then update the regularization factor as follows:

$$\lambda_{n+1} = \begin{cases} \lambda_n & p_n < 1 \\ \lambda_n / p_n & p_n > 1 \end{cases}. \tag{27}$$

If the misfit functional is not shrinking fast enough, namely $\| \boldsymbol{r_n^{\omega_n}} \|^2 - \| \boldsymbol{r_{n+1}^{\omega_{n+1}}} \|^2 < 0.01 \| \boldsymbol{r_n^{\omega_n}} \|^2$, the value of λ_{n+1} calculated by Equation (27) should be reduced to q times of the original value ~~and we~~

selected q=0.6 ~~according to experience~~. It is not difficult to find that for the solution obtained in each iteration, if the value of regularization parameter is continuously reduced, the value of the corresponding objective functional also keeps decreasing, which guarantees the objective functional can converge faster on the premise of obtaining a stable solution.

When the misfit reaches a given range:

$$Misfit = \frac{\|\boldsymbol{Am_N - d}\|}{\|\boldsymbol{d}\|}.100\% \leq \varepsilon_0, \quad (28)$$

the iteration process terminates and output $\boldsymbol{m_N}$, otherwise proceed to the next iteration.

3. Synthetic Examples

We examined the feasibility and effectiveness of 3D regularized focusing migration with several typical synthetic models. First, we designed a single cube with a ~~residual~~ density of 1 g/cm^3, located at a depth of 150 m ~~at the center~~. The three-dimensional diagram of the subsurface model and its surface gravity anomalies are shown in Figures 2(a) and (b). The subsurface inversion domain was divided into 50 × 50 × 25 regular ~~grids~~.

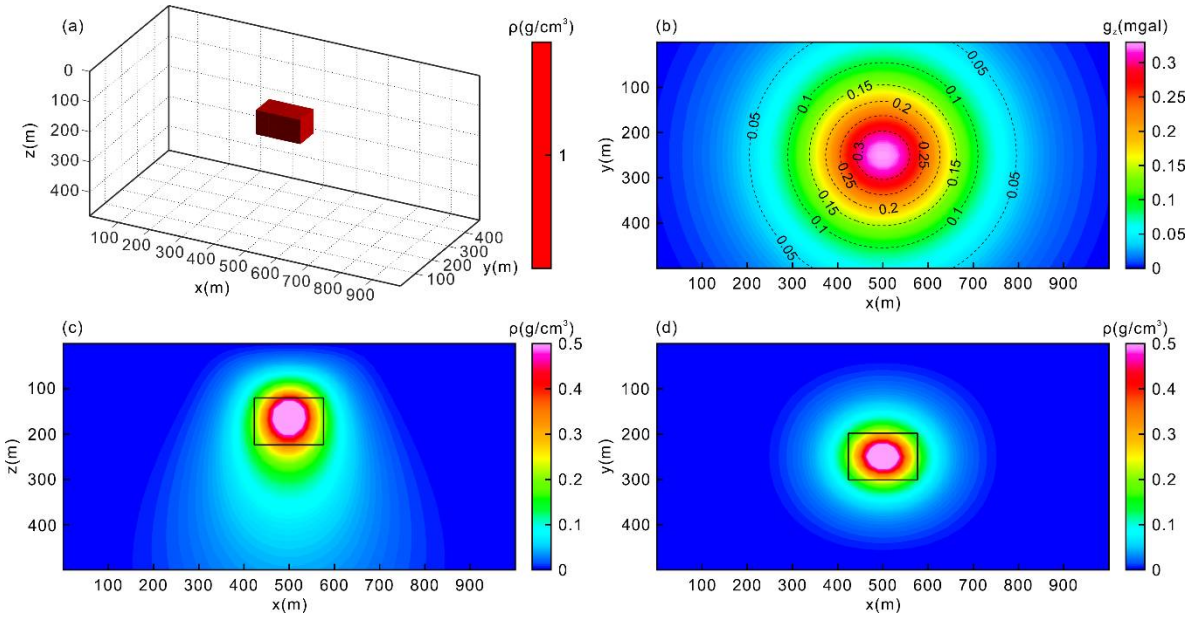


Figure 2. (a) Three-dimensional diagram of ~~the~~ single cube model; (b) gravity anomal~~ies~~ on the groun~~d~~ generated from the model; (c) vertical cross-sectio~~n of~~ y=250m obtained from 3D regularized focusing migration; (d) horizontal cross-section of z=150m obtained from 3D regularized focusing migration.

Figures 2 (c) and (d) show the cross-sections ~~of~~ the regularized focusing migration ~~results~~ at y = 250m and z = 150m respectively. The density extremum of the imaging results corresponded well with the center of the abnormal body, and high density distribution precisely outlined the anomalous body, manifesting the feasibility of the method.

~~Then we considered a model formed by dike complex and a rectangle.~~ Figure 3(b) shows the gravity anomaly ~~generated~~ by ~~the~~ model ~~shown in Figure 3(a)~~.

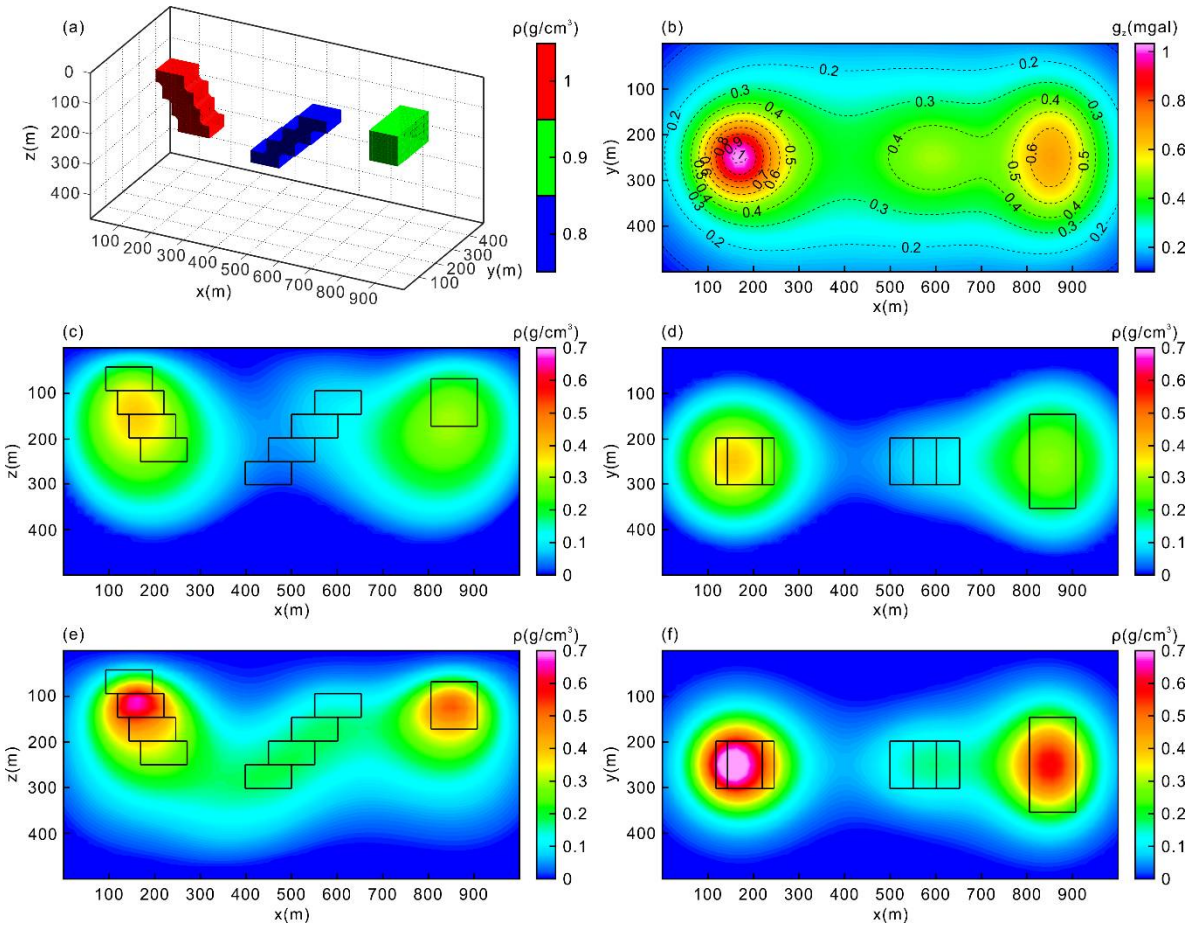


Figure 3. (a) Three-dimensional ~~diagram~~ of the subsurface model; (b) gravity anomalies on the ground generated from the model; (c) vertical cross-section of y=250 m obtained from conventional iterative migration; (d) horizontal cross-section of z=150 m obtained from conventional iterative migration; (e) vertical cross-section of y=250 m obtained from 3D regularized focusing migration; (f) horizontal cross-section of z=150 m obtained from 3D regularized focusing migration.

Figures 3(c)-(f) show the cross-sections of density ~~results~~ obtained by conventional iterative migration and regularized focusing migration. Regularized focusing migration method ~~could divide~~ the trend of the dikes, ~~of which the result was more~~ convergent ~~and closer to actual conditions, and imaging for the bottom of the model remained accurate in deep locations~~. Whereas the conventional iterative migration method barely distinguished three ~~abnormal~~ bodies and underestimated the ~~sloping~~ dikes, showing divergent density distribution that was far beyond the actual extent. In ~~particular~~, 3D regularized focusing migration ~~had~~ a better spatial resolution and preserved sharper and finer boundaries.

Next, we investigated how regularized focusing migration performs for noise conditions. Figure 4(a) shows the three-dimensional diagram of ~~independent~~ cubes with ~~residual~~ density of 1 g/cm^3, located at depths of 70 m and 100 m. Figure 4(b) shows the surface gravity anomalies ~~generated by the complex model sets~~. We added 5% random Gaussian noise to the observed gravity data, shown in Figure 4(c), to simulate the data collected in actual surveys. The imaging results of noiseless and noise-corrupted data are shown in Figures 4(d)-(g). The imaging results for both noiseless and noise-corrupted data were in good agreement with the true model even when geological bodies were close. The extremum of density distribution corresponded well to the center of each geological body, and horizontal positions and buried depths could be clearly delineated~~, although the density result was somewhat different from the actual conditions, especially for the geological bodies in a deeper position~~. It ~~was~~ apparent that the direct imaging of noise-containing data still produced stable and smooth results, and density distribution was not obviously serrated. We also ~~exhibited~~ the volume

image with a density cut-off greater than 0.3 g/cm³ of noiseless and noise-containing data, as shown in Figure 4 (h) and (i), respectively. ~~It could be seen that the~~ result of direct migration of noise-containing data ~~hardly changed compared with~~ that of noiseless data. ~~It's demonstrated~~ that the regularized focusing migration method ha~~d~~ good noise resistance since the introduction of a regularization term prevents local overfitting. ~~It had~~ good ~~generalization~~ performance and ~~could~~ obtain global optimal results.

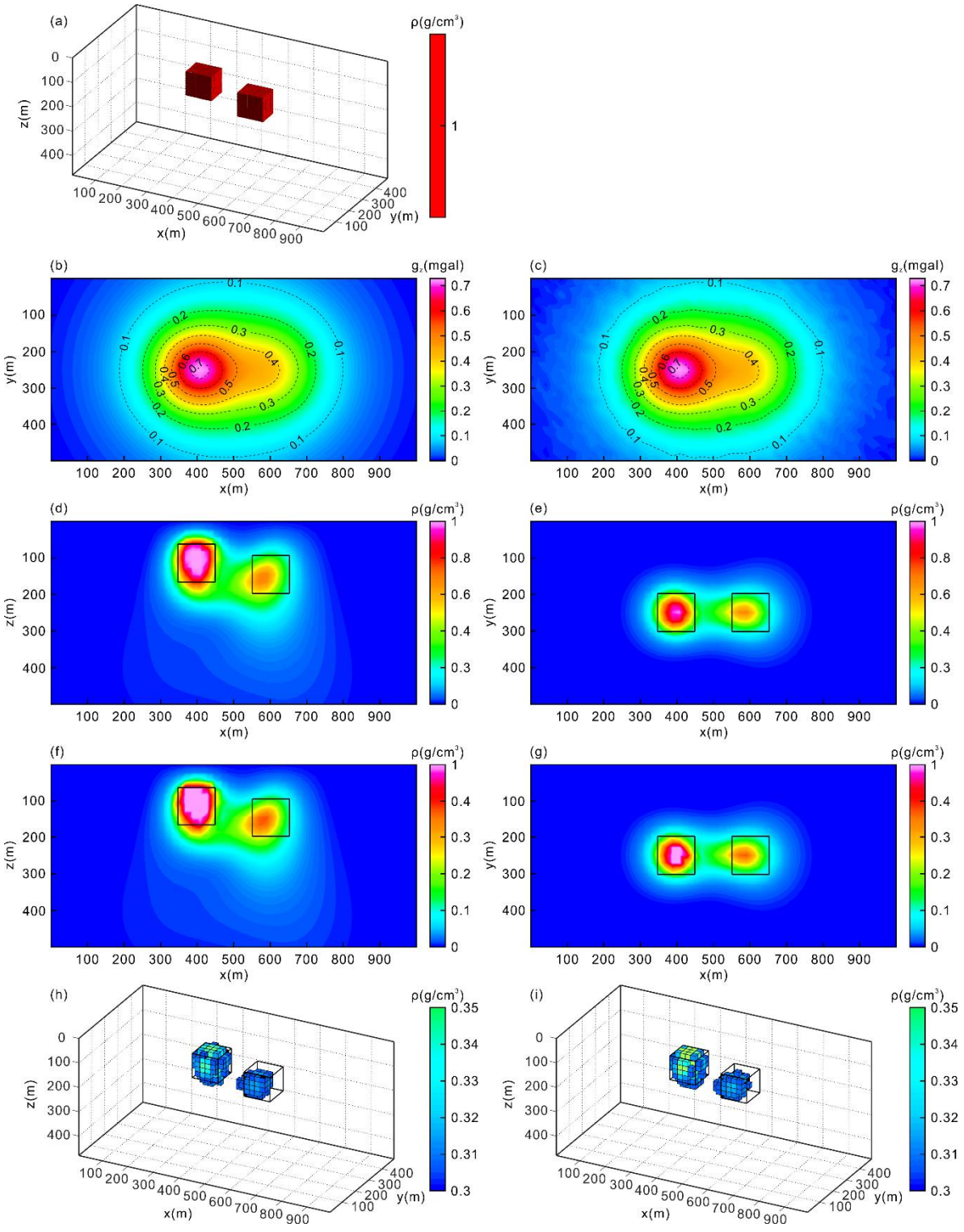


Figure 4. (a) Three-dimensional diagram of the subsurface model; (b) gravity anomalies on the ground generated from the model; (c) gravity anomalies on the ground generated from the model with 5% random Gaussian noise added; (d) vertical cross-section of y=250 m for noiseless gravity data; (e)

horizontal cross-section of z=150 m for noiseless gravity data; (f) vertical cross-section of y=250 m for noise-corrupted data; (g) vertical cross-section of z=150 m for noise-corrupted data; (h) volume image with a density cut-off greater than 0.3 g/cm^3 for noiseless data; (i) volume image with a density cut-off greater than 0.3 g/cm^3 for noise-corrupted data.

Finally, we analyzed the efficiency of the proposed method. The model shown in Figure 2(a) was adopted. Figure 5 shows the misfit curves ~~with~~ the number of iteration ~~of~~ regularized inversion, conventional iterative migration method and our proposed method. The migration method ~~could~~ obtain a result ~~that showed~~ a lower misfit in the first iteration, ~~so as to get the relatively~~ convergent ~~result~~ faster and ~~reduce~~ calculation time. Numerical results presented that our method could decrease the iterative number by 35% and greatly reduce computation time.

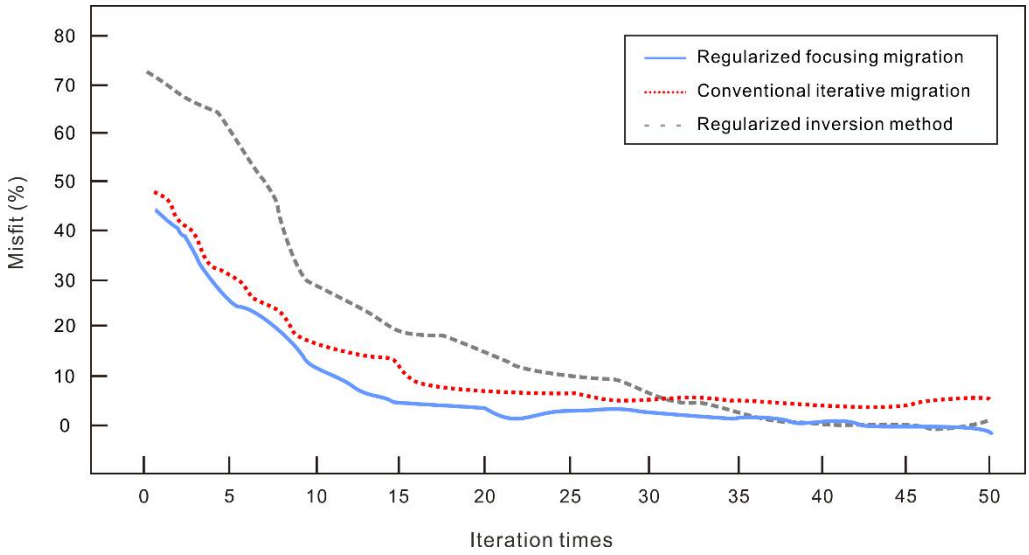


Figure 5. Misfit ~~with iteration number~~ of three different methods: regularized focusing migration, conventional iterative migration and regularized inversion.

Figure 6 shows the computation time of regularized focusing migration method ~~with~~ the model scale. The iteration process stopped when the misfit reached a 5% data error level. ~~It was indicated that~~ for models less than 6 × 6 × 6 cells, the computation time for both line search criterion is constant because the model scale is relatively small and most of the time is spent on the ~~domination by~~ initialization work. For models ~~exceeding~~ 6 × 6 × 6 cells, there is a linear dependency of computation time on the model scale. For computations based on Wolfe-Powell conditions, time consumption is higher than that of the exact line search with models under 16 × 16 × 16 cells, but ~~the situation is reversed with~~ models exceeding 16×16×16 cells. This is because the exact line search for each step involves in the calculation of $\boldsymbol{A}_{\alpha}^{\omega}\boldsymbol{A}_{\alpha}^{\omega *}$, which means that time complexity grows roughly as $(n_x.n_y)^2(n_x.n_y.n_z)^2$, while for the Wolfe-Powell conditions, which mainly calculate $\boldsymbol{A}_{\alpha}^{\omega}\boldsymbol{m}$ multiple times each time the step size is determined, time complexity is approximately $n_x{}^2 n_y{}^2 n_z$. The solution of the underdetermined system of equations does not depend on the exact search process. When the model scale is too large, the cost of using the exact line search is relatively high. According to Wolfe-Powell conditions, global convergence is expected to be fast. Although ~~the~~ number of steps increases, convergence speed is accelerated.

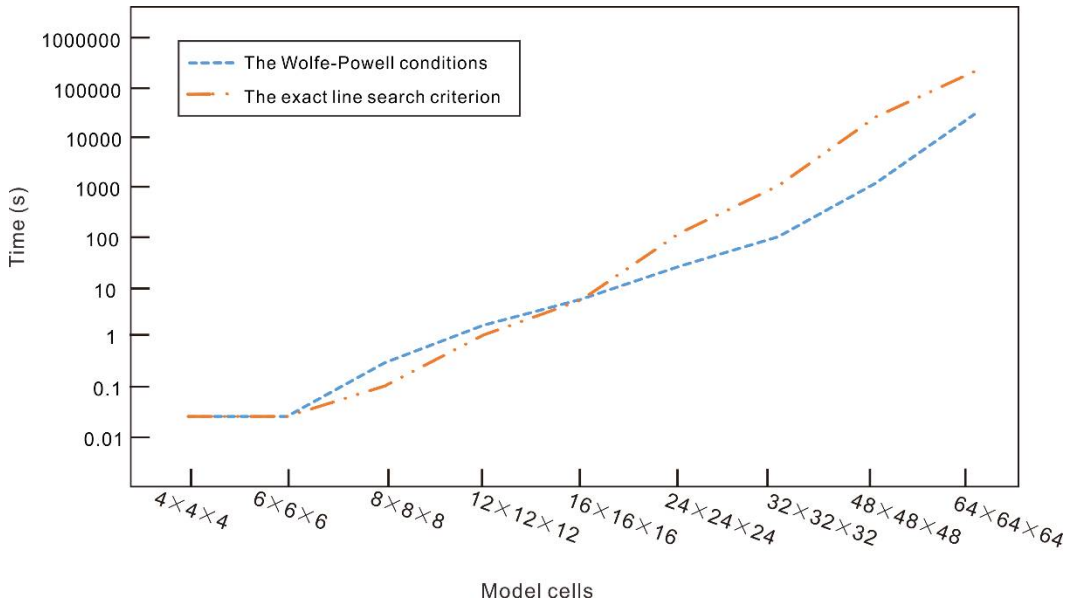


Figure 6. Computation time of regularized focusing migration method for models ~~with different cells~~. Blue solid line represents using the Wolfe-Powell line search conditions, and red solid line ~~represents using~~ exact line search criterion shown in Equation (9).

It should be noted that our novel method only took 224 s ~~for~~ processing ~~with a~~ model ~~scale~~ of 50 × 50 × 25 cells. Compared with other inversion algorithms, it is indeed an encouraging speed. This efficiency is due to adopting the conjugate migration direction and the step size based on the Wolfe-Powell conditions when updating the model parameters during each iteration. Besides, the continuous decrease of the regularization parameter and the introduced focusing weight can also accelerate convergence ~~to quickly~~ obtain a solution that minimizes the objective functional. Therefore, when studying regional structure and deep geological problems, regularized focusing migration imaging can be used for global analysis without ~~the~~ need for data thinning. This is especially applicable to the investigation of large-scale mining areas, as in the subsequent case study of the Yucheng mining area, Shandong, China.

4. Field example

In 2011, Shandong Province Mineral Resources Potential Evaluation Project ~~raised~~ that the Yucheng area had considerable metallogenic conditions of skarn-type ore deposits. In the following years, a variety of geological surveys showed that the area had good prospecting ~~future~~, and iron ore bodies were ~~exposed~~ during drilling. Some traditional interpretation of geophysical surveys in this area was based on analysis of contour maps of gravity or magnetic anomaly [31,32,33], which provided the major geophysical ~~features~~ of the area and could be used to determine the approximate extent of the deposits. However, they alone could not determine the exact location and depth of the mineral deposits.

In the following sections, we first summarize the metallogenic geological conditions ~~in~~ this area, then use our high-resolution method to invert the results of entire airborne gravity data into 3D density models, and finally analyze the density imaging results ~~based on~~ the relevant geological information to identify potential mining targets. Our work provides reference for the ~~ground~~ follow-up and exploration of skarn-type iron ore under thick overburden.

4.1. Geological Background of Survey Area

The survey area is ~~on~~ Qihe county - Yucheng county border ~~in~~ the south of Dezhou city, Shandong province, and belongs to the plain of northwestern Shandong. It is located on the Luxi uplift~~ed~~ area of the North China plate tectonically (Figure 7) [34]. The area is covered by the strata of Cambrian, Ordovician, Carboniferous, Permian, Neogene and Quaternary from the base to the top

[31]. The surface is completely covered by thick Quaternary and Neogene ~~strata~~, without any bedrock outcrops [35]. All kinds of deep geological information are inferred from geophysical data. Affected by regional tectonic movements, fault structures widely developed, including NE-striking faults, NNW-striking faults and SN-striking faults, and fold structures locally developed (Figure 8).

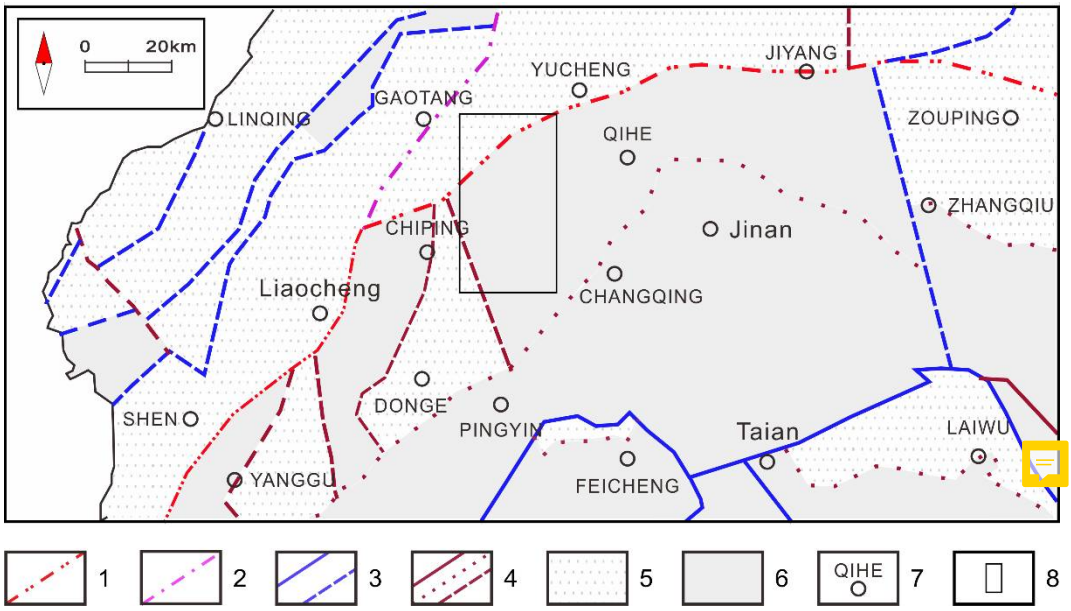


Figure 7. Tectonic background map of Yucheng area. The survey area is outlined as the black rectangle. 1-The secondary structural unit; 2-the tertiary structural unit; 3- the quaternary structural unit; 4-five-level structural unit; 5-(latent) sag zone; 6-(latent) high zone; 7-toponym; 8- survey area.

Skarn-type iron ores in this region are generally characterized by the joint control of strata, intrusive rocks and structures. The ~~strata of the~~ Ordovician Majiagou group ~~carbonate rocks~~ are widely distributed and ~~are important ore-controlling~~ host rocks ~~of~~ skarn-type iron ores. In addition, some iron-ore bodies also occur in the ~~strata~~ of the Carboniferous-Permian ~~clastic rocks~~. According to available borehole data, the Ordovician strata ~~are buried deeper on~~ the northwest reaching 3440 m or more, while ~~the buried depths of the Ordovician strata vary~~ greatly in the southeastern area, ~~among which the buried depths in the east of~~ Litun and in the northwest of Dazhang ~~are about 1165 m and 610–650 m,~~ respectively. There is no borehole data in the northwest of Pandian, and the depth of the Ordovician ~~strata~~ is unknown [35]. In the survey area, magmatic activity during late Yanshanian was violent, and igneous rock ~~mass was relatively developed at the intersections of the structures~~. The investigation of iron ore indicates the ~~occurrence~~ types of iron-ore bodies are ~~diverse, of which~~ the contact zone ~~occurrence is the main type, and the ore bodies occur near the contact zone~~ between the body mass of late Yanshanian intermediate-basic intrusive rocks that dominated by diorite and gabbro and the state of Ordovician limestone ~~rocks~~. In addition, some ore bodies occur in the interjunction of fault structures and xenoliths near the rock mass [33].

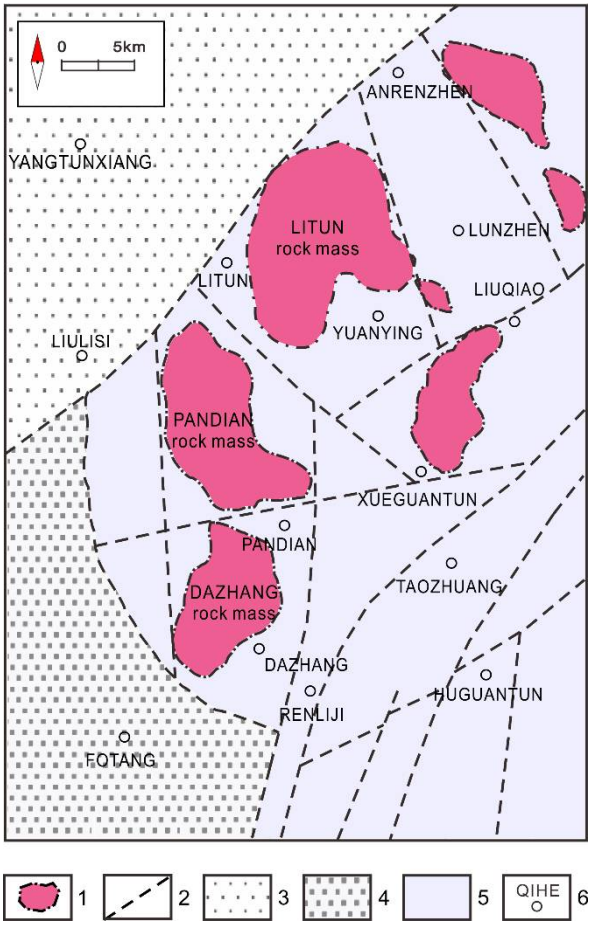


Figure 8. Geological map of the survey area. The figure is from [34]. 1-Inferred range of concealed diorite rocks; 2-inferred concealed fault; 3-Yucheng-Jiyang latent sag; 4-Lepingpu latent sag; 5-Qihe latent high; 6-toponym.

4.2. Data Acquisition

The airborne gravity survey collected gravity data was performed in Yucheng area, Shandong by the China Aero-Geophysical Survey and Remote Sensing Center for Land and Resources (AGRS). During the survey, a gravimeter was installed in the cabin of a CESSNA208 aircraft. The flight altitude was fixed at 450 m above ~~sea~~. The 45 × 35 km^2 survey area was flown at 1500 m line spacing. The flight survey lines were designed to be perpendicular to the regional geological strike to ensure an effective sampling ~~rate~~. Figure 9 shows the gravity survey lines in Yucheng area and the black rectangle delineates the ~~area~~ where we perform regularized focusing migration.

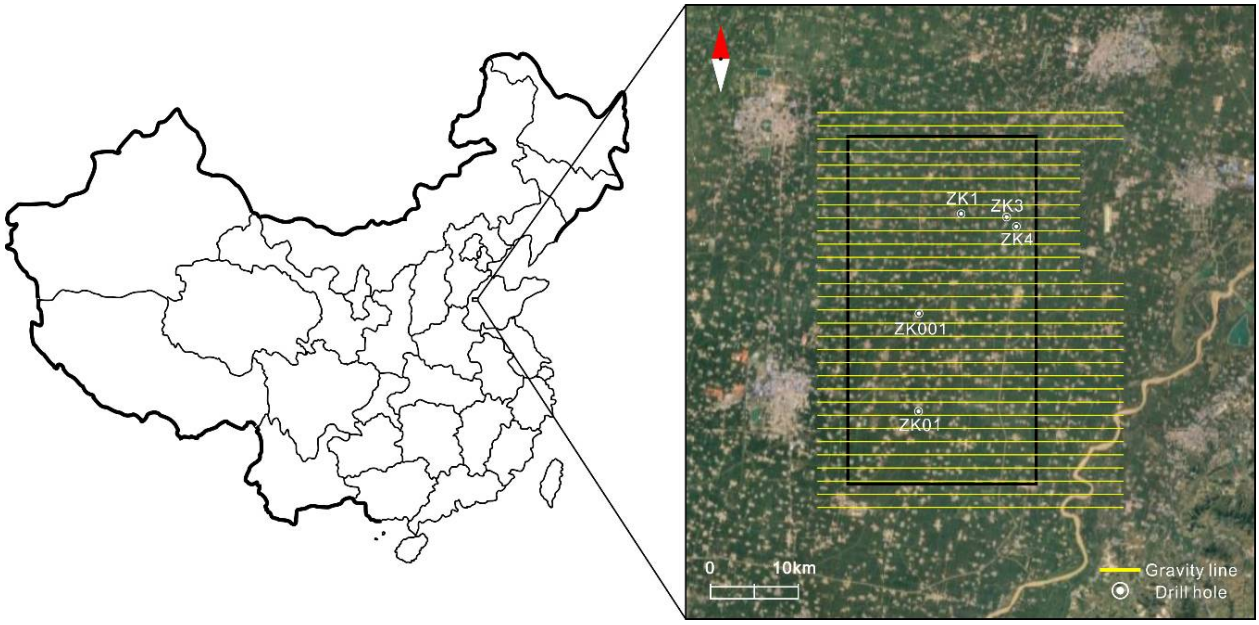


Figure 9. Gravity survey lines in Yucheng area. The black rectangle shows the ~~area where we performed~~ regularized focusing migration.

4.3. Migration Models of Gravity Data

We performed terrain correction, normal field correction, and Bouguer correction on the collected gravity data to obtain Bouguer gravity anomalies (Figure 10(a)). The characteristics of regional gravity anomalies generally reflected the distribution of late Yanshanian intrusive rocks and the Ordovician strata uplift in the region. The iron-ore deposits ~~to predict were mainly located above~~ 2 km ~~underground~~, since iron ore below ~~had~~ no economic mining value. The regional field below 2 km was separated from the Bouguer gravity anomaly by matched filtering [36], thus weakening the influence of deep structures on the ~~imaging results of shallow density migration.~~ Figure 10(b) shows the radial logarithmic power spectrum of the Bouguer gravity anomaly. Long-wavelength anomalies were removed to obtain the shallow local gravity anomalies~~, as shown in~~ Figure 10(c), ~~where~~ three main ~~portions of~~ high ~~value of local gravity anomaly could be seen:~~ Dazhang, Pandian and Litun anomaly areas. Four wells were drilled, including three holes in Litun area and one ~~hole~~ in Yucheng area, among which the ZK1 well in Litun area and the ZK001 well in Dazhang area ~~are~~ discoveries ~~with~~ rich magnetite bodies (Tables 1 and 2). According to ~~existing~~ borehole data, the density of magnetite was significantly higher than other rocks.

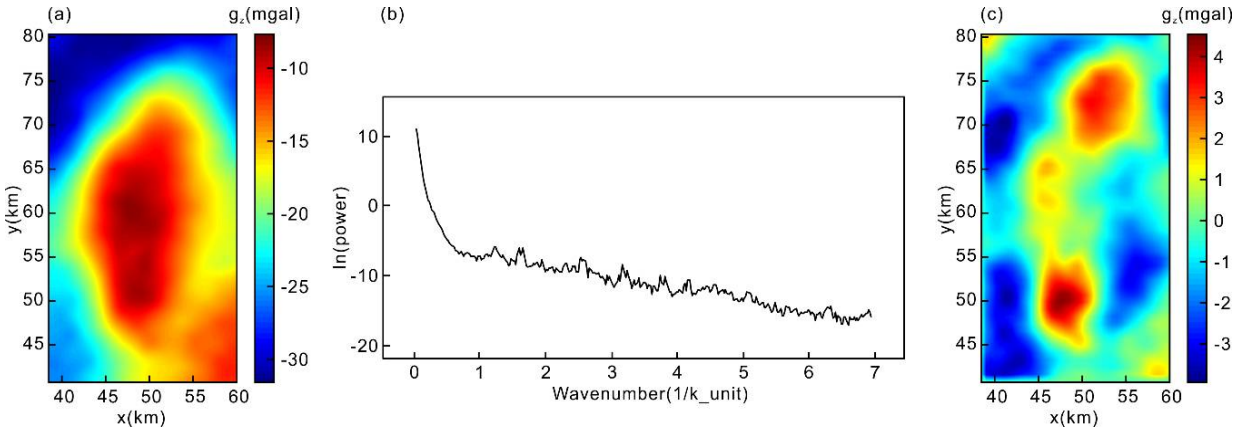


Figure 10. (a) Regional gravity anomaly; (b) radial logarithmic power spectrum; (c) local gravity anomaly.

Table 1. Dazhang ZK003 drilling data.

Lithology	Top Surface Depth (m)	Thickness (m)	Density (g/cm³)
Sand/mealy sand/clay	0	571.9	
Mudstone/sandstone/ limestone	571.9	18.4	2.69
Limestone	590.3	19.1	2.68
Limestone	609.4	103.7	2.72
Diorite	713.1	86.3	2.64
Skarn	799.4	2.6	3.15
Magnetite	802	15.3	4.41
Skarn	817.3	2.4	3.18
Magnetite	819.7	0.6	4.45
Diorite	820.3	105.7	2.63

Table 2. Litun ZK1 drilling data.

Lithology	Top Surface Depth (m)	Thickness (m)	Density (g/cm³)
Sandstone/mudstone	0	1126.19	
Diorite	1126.19	19.03	2.57
Skarn dolomite	1145.22	5.02	2.66
Skarn	1150.24	7.14	2.87
Magnetite	1157.38	9.34	4.19
Skarn	1166.72	3.15	2.82
Magnetite	1169.87	8.77	4.26
Crushed zone	1178.64	5.31	
Skarn	1183.95	14.39	2.84
Magnetite	1198.34	98.15	4.49
Skarn	1296.49	16.35	2.87
Diorite	1312.64	123.46	2.68

Combining the stratigraphic, magmatic rocks distribution characteristics with the drilling data in the survey area, the high values of local gravity anomalies were mainly caused by the skarn-type magnetite deposits. The positive density contrast of the migration imaging results could be ~~regarded~~ as a sign of a prospecting criterion. We performed regularized focusing migration imaging of local gravity anomalies with an initial model based on drilling data, and then delineated the spatial distribution of the iron ore under the range of positive density contrast of the imaging results. The local gravity data were inverted in a region designed as 21500 m × 39600 m in the X and Y directions and 2 km in Z direction, with 88 × 98 × 50 small cells. Figure 11 shows a perspective view of the migration density model with abnormal parts with a density greater than 0.7 g/cm³, which gives a transparent view for ~~abnormal materials~~. For better representation, horizontal cross-sections with different depths are shown in Figure 12.

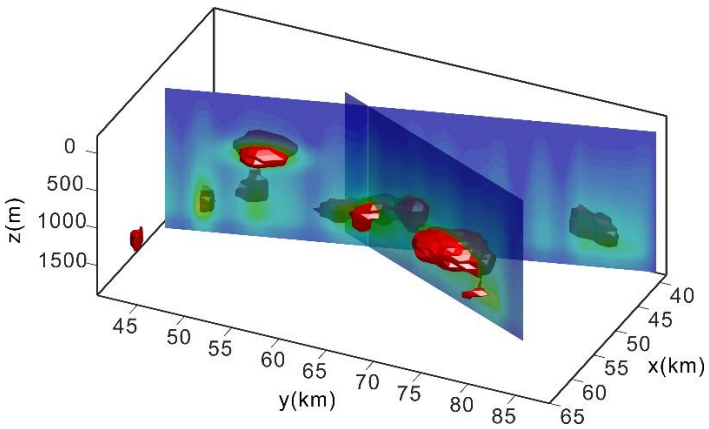


Figure 11. Perspective view of the migration density model. Red anomalous body shows density distribution with density greater than 0.7 g/cm³.

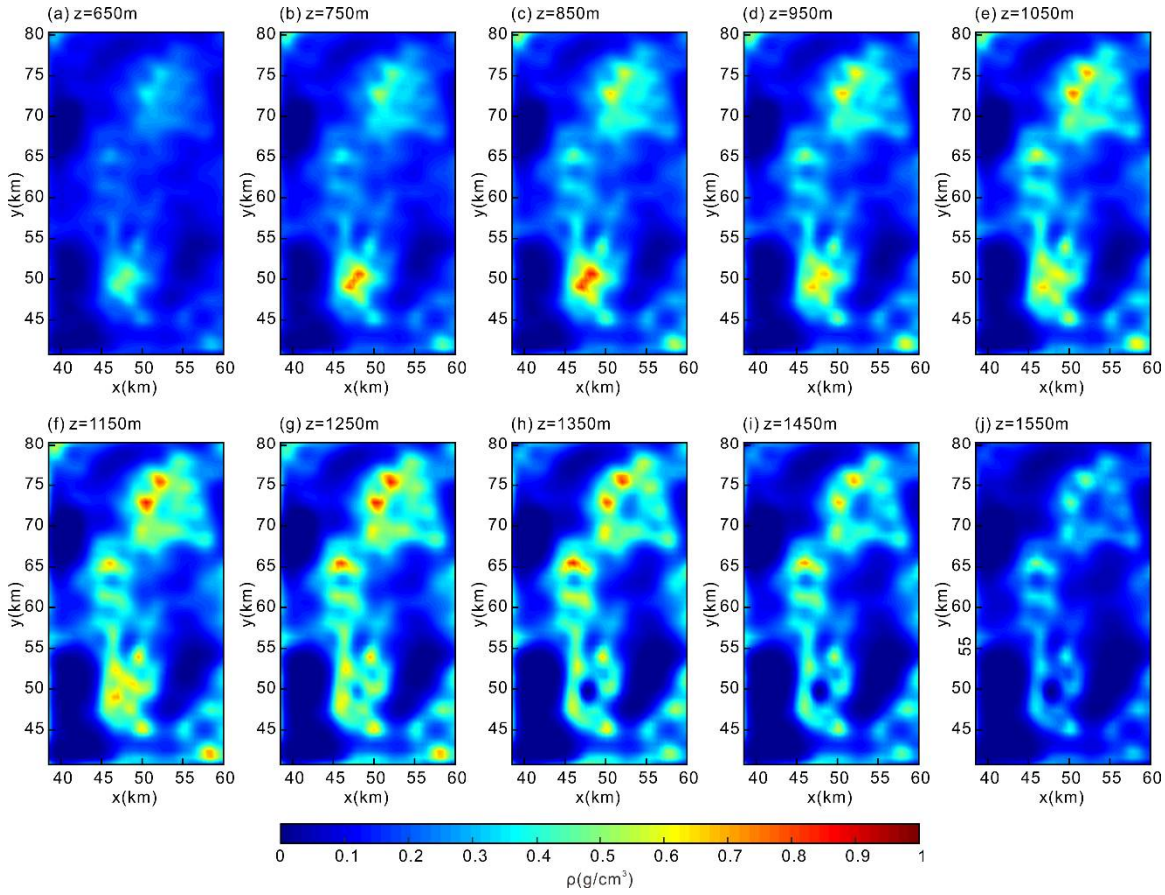


Figure 12. Horizontal cross-sections at different heights of imaging results.

4.4. Geological Interpretation of the Mining Area

Migration imaging ~~results show that there is~~ considerable potential for mineral resources underneath Litun, Pandian and Dazhang anomaly areas. Ore bodies are mainly distributed ~~below~~ 700 m and ~~above~~ 1500 m ~~underground~~.

~~The~~ ore-body distribution ~~range is delineated based on the high density results, as shown in Figure 13, whose bottom layer is~~ a simplified geological map of the survey area. One can see that the target mineralized zones are mainly concentrated in the vicinity of fault structures since faults can provide channels for magmatic upwelling ~~and the rock mass is well developed at the junction of structures as a result~~. The iron ore buried depth of Litun (Ⅰ) is about 1050 m-1350 m, that of Pandian (Ⅱ, Ⅲ) is about 1150 m-1550 m, and that of Dazhang (Ⅳ) is about 750 m-950 m. It should be noted that the Pandian area (Ⅱ, Ⅲ) is rich in iron ore resources underground, whereas these resources are deeper and less extensive, and the drilling will be more difficult than the that in the Litun (Ⅰ) and Dazhang areas (Ⅳ). The Litun and Dacheung areas contain low-hang ing fruit of the survey area and should be set as key prospecting drilling areas. When these targets are exhausted and more geological information is obtained, exploration can proceed outward, including under the Pandian area along with other nearby high density distributions that have not yet been measured.

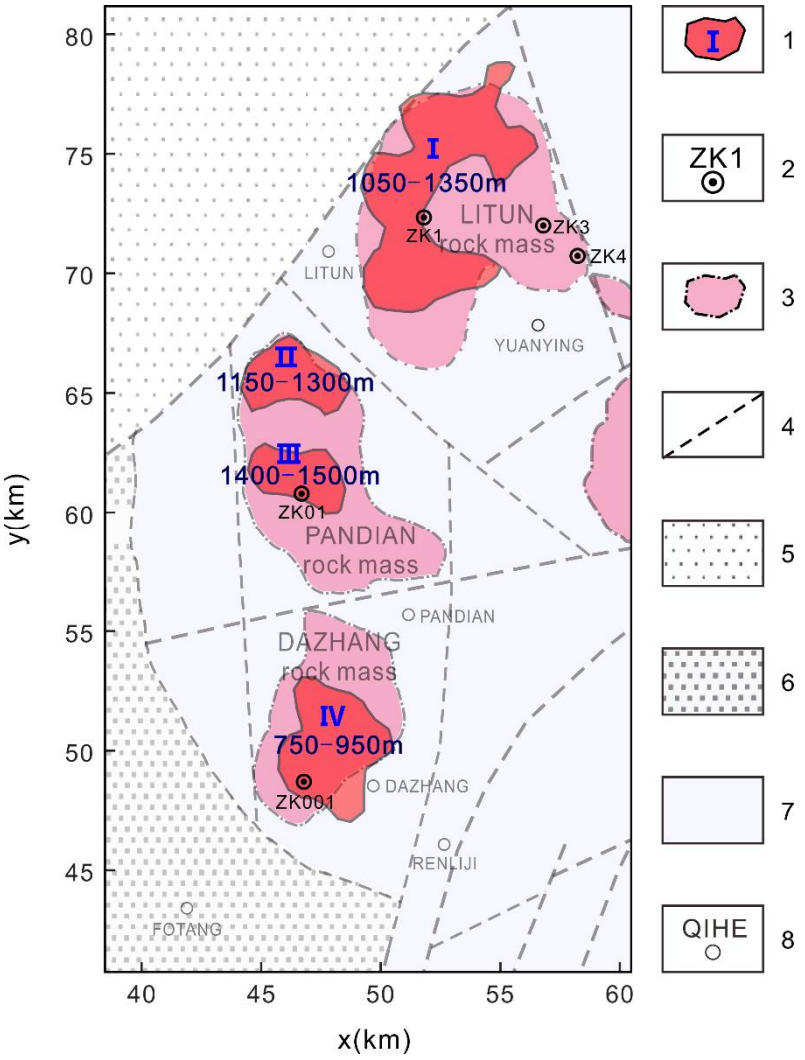


Figure 13. Map of iron ore range corendered with corresponding geological map. 1- Scope of prospecting target area; 2-drill hole; 3-inferred range of concealed diorite rocks; 4- inferred concealed fault; 5- Yucheng-Jiyang latent sag; 6-Lepingpu latent sag; 7-Qihe latent high; 8- toponym.

~~Also encouraging, the newly drilled~~ well (ZK01) in this area found ~~an~~ iron mine ~~with a thickness of 54.4 m below 1444.4~~ m, which ~~was~~ consistent with ~~the~~ interpretation ~~by our method~~. ~~R~~egularized focusing migration method has the ability to delineate the horizontal range of orebody, predict mineral depth and ~~locate the target prospecting area~~.

5. Conclusions

We have developed 3D regularized focusing migration of large-scale gravity data with higher horizontal and vertical resolution compared ~~with~~ conventional gravity migration imaging. Validated by synthetic models, this method can resolve complicated geological structures and has high stability in noise conditions. Meanwhile the proposed algorithm based on the conjugate migration direction and the Wolfe-Powell conditions inherits the high efficiency of conventional migration and can ~~obtain~~ real-time imaging with high accuracy. This provides a ~~reference for the study of~~ deep mineral resources, ~~as the ore bodies are mostly concentrated in relatively~~ high density.

We have shown how this method can be ~~productively~~ used for ~~the~~ interpretation of the airborne gravity data collected over the Yucheng mining area, Shandong, China. High-resolution imaging results were obtained for high-density body distribution. ~~Results~~ helped identify several potential mining targets ~~that usually have~~ no surface expression ~~and~~ can only be detected ~~using~~ modern high-resolution geophysical methods. Currently, one of the predicted targets ~~shown here~~ is undergoing

further drilling exploration based on these airborne gravity analyses and well results so far coincide with our predictions. This method offers a ~~reference~~ for follow-up exploration in this area ~~so as to provides a road~~ map ~~for~~ skarn-type iron ore ~~exploration~~ under thick overburden.

We have learned that iron-ore anomalies in this area have gravity and magnetic homology characteristics. Gravity and magnetic combination inversion will subsequently be used in this area to reduce the non-uniqueness of the results. Joint inversion of multiple geophysical data is the focus of our future research.

Author Contributions: conceptualization, Yidan Ding and Guoqing Ma; data curation, Yidan Ding and Guoqing Ma; formal analysis, Yidan Ding; funding acquisition, Guoqing Ma; investigation, Yidan Ding; methodology, Yidan Ding; project administration, Guoqing Ma; resources, Shengqing Xiong; software, Yidan Ding and Haoran Wang; supervision, Guoqing Ma; validation, Yidan Ding; visualization, Yidan Ding; writing – original draft, Yidan Ding; writing – review & editing, Guoqing Ma.

Funding: This research was funded by the National Key Research and Development Program of China, grant numbers 2017YFC0602203 and 2017YFC0602000.

Conflicts of Interest: The authors declare no conflict of interest.

References

1. Tikhonov, A.N. Regularization of incorrectly posed problem. *Sov. Math. Dokl.* **1963**, *4*, 1624–1627.
2. Phillips, D.L. A technique for the numerical solution of certain integral equations of the first kind. *J. ACM* **1962**, *9*, 84–97.
3. Strakhov, V.N. The solution of linear ill-posed problems in Hilbert space. *Differentsial'nye Uravneniya* **1970**, *6*, 1490–1495.
4. Lavrent'ev, M.M.; Romanov, V.G.; Shishatskii S.P. *Ill-Posed Problems of Mathematical Physics and Analysis*, 1st ed.; American Mathematical Society: Providence, RI, USA, 1986; pp. 290–299.
5. Li, Y.; Oldenburg, D.W. 3-D inversion of gravity data. *Geophysics* **1998**, *63*, 109–119.
6. Li, Y. 3-D inversion of gravity gradiometer data. In *SEG Technical Program Expanded Abstracts*; Society of Exploration Geophysicists: San Antonio, TX, USA, 1999; pp. 1470–1473.
7. Van Zon, T.; Roy-Chowdhury, K. Structural inversion of gravity data using linear programming. *Geophysics* **2006**, *71*, 41–50.
8. Zou, H.; Hastie, T. Regularization and variable selection via the elastic net. *J. R. Stat. Soc. Ser. B* **2005**, *67*, 301–320.
9. Martins, C.M.; Lima, W.A.; Barbosa, V.C.; Silva, J.B. Total variation regularization for depth - to-basement estimate: Part 1—Mathematical details and applications. *Geophysics* **2011**, *76*, I1–I12.
10. Lima, W.A.; Martins, C.M.; Silva, J.B.; Barbosa, V.C. Total variation regularization for depth-to-basement estimate: Part 2—Physicogeologic meaning and comparisons with previous inversion methods. *Geophysics* **2011**, *76*, I13–I20.
11. Last, B.J.; Kubik, K. Compact gravity inversion. *Geophysics* **1983**, *48*, 713–721.
12. Portniaguine, O.; Zhdanov, M.S. Focusing geophysical inversion images. *Geophysics* **1999**, *64*, 874–887.
13. Wahba, G. Spline models for observational data. *Technometrics* **1990**, *34*, 113–114.
14. Hansen, P.C. *Rank-Deficient and Discrete Ill-Posed Problems: Numerical Aspects of Linear Inversion*, 2ed ed.; The Society for Industrial and Applied Mathematics: Philadelphia, PA, USA, 1998; pp. 69–87.
15. Akaike, H.; Parzen, E.; Tanabe, K. *Selected Papers of Hirotugu Akaike*, 1st ed.; Springer Science and Business Media: New York, NY, USA, 1980; pp. 309–332.
16. Zhang, R.; Li, T.; Zhou, S.; Deng, X. Joint MT and gravity inversion using structural constraints: A case study from the Linjiang copper mining area, Jilin, China. *Minerals* **2019**, *9*, 407.
17. Farquharson, C.G.; Oldenburg, D.W. A comparison of automatic techniques for estimating the regularization parameter in non-linear inverse problems. *Geophys. J. Int.* **2004**, *156*, 411–425.
18. Zhdanov, M.S.; Liu, X.; Wilson, G.A. Rapid imaging of gravity gradiometry data using 2D potential field migration. In *SEG Technical Program Expanded Abstracts*; Society of Exploration Geophysicists: Denver, CO, USA, 2010; pp. 1132–1136.
19. Zhdanov, M.S.; Liu, X.; Wilson, G. Potential field migration for rapid 3D imaging of entire gravity gradiometry surveys. *First Break* **2010**, *28*, 47–51.

20. Zhdanov, M.S.; Liu, X.; Wan, L.; Čuma, M.; Wilson, G.A. 3D potential field migration for rapid imaging of gravity gradiometry data—A case study from Broken Hill, Australia, with comparison to 3D regularized inversion. In *SEG Technical Program Expanded Abstracts*; Society of Exploration Geophysicists: San Antonio, TX, USA, 2011; pp. 825–829.
21. Zhdanov, M.S.; Liu, X.; Wilson, G.A.; Wan, L. Potential field migration for rapid imaging of gravity gradiometry data. *Geophys. Prospect.* **2011**, *59*, 1052–1071.
22. Wan, L.; Zhdanov, M.S. Iterative migration of gravity and gravity gradiometry data. In *SEG Technical Program Expanded Abstracts*; Society of Exploration Geophysicists: Houstun, TX, USA, 2013; pp. 1211–1215.
23. Wan, L.; Han, M.; Zhdanov, M.S. Joint iterative migration of surface and borehole gravity gradiometry data. In *SEG Technical Program Expanded Abstracts*; Society of Exploration Geophysicists: Houstun, TX, USA, **2016**; pp. 1607–1611.
24. Zhdanov, M.S.; Ellis, R.; Mukherjee, S. Three-dimensional regularized focusing inversion of gravity gradient tensor component data. *Geophysics* **2004**, *69*, 925–937.
25. Portniaguine, O.; Zhdanov, M.S. 3-D magnetic inversion with data compression and image focusing. *Geophysics* **2002**, *67*, 1532–1541.
26. Wolfe, P. Convergence conditions for ascent methods. *SIAM Rev.* **1969**, *11*, 226–235.
27. Powell, M.J.D. *Some Global Convergence Properties of a Variable Metric Algorithm for Minimization without Exact Line Searches*, 1st ed.; SIAM publications: Philadelphia, PA, USA, 1976; pp. 53–72.
28. Forsberg, R.; Tscherning, C.C. The use of height data in gravity field approximation by collocation. *J. Geophys. Res. Solid Earth* **1981**, *86*, 7843–7854.
29. Zhdanov, M.S. *Geophysics Inverse Theory and Regularization Problems*, 1st ed.; Elsevier Science B.V.: Amsterdam, The Netherlands, 2002; pp. 186–197.
30. Lemaréchal, C. A view of line-searches. In *Optimization and Optimal Control*, 1st ed.; Springer: Berlin/Heidelberg, Germany, 1981; pp. 59–78.
31. Cheng, X.; Wang J.; Wang J.; Zhai, D.; Cai, T. Geological characteristics and prospecting potential of Dazhang iron deposit in Qihe County of Shangdong Province. *Shandong Land Resour.* **2017**, *33*, 24–29.
32. Guo, Y.; Hao, X.; Zhong, W.; Ru, L.; Zhao, C. Application of high-precision magnetic measurement in exploration of hidden iron deposit: Setting iron deposits in Litun area of Yuchen City in Shandong Province as an example. *Shandong Land Resour.* **2017**, *33*, 52–56.
33. Hao, X.; Yang, Y.; Li, Y.; Gao, H.; Chen, L. Ore-controlling characteristics and prospecting criteria of iron deposits in Qihe area of western Shandong. *J. Jilin Univ.* **2019**, *49*, 982–991.
34. Kong, Q.; Zhang, T. *Deposits of Shandong*, 1st ed.; Shandong Science and Technology Press; Jinan, China, 2006; pp. 64–71.
35. Hao, X.; Liu, W.; Zang, K.; Zhang, X. Primary study on metallogenic regularity of skarn type iron deposit in Pandian area in weatern Shandong Province. *Shandong Land Resour.* **2018**, *34*, 27–33.
36. Syberg, F.J.R. A Fourier method for the regional—Residual problem of potential fields. *Geophys. Prospect.* **1972**, *20*, 47–75.



© 2020 by the authors. Submitted for possible open access publication under the terms and conditions of the Creative Commons Attribution (CC BY) license (http://creativecommons.org/licenses/by/4.0/).